Effects of surface modifications on the fatigue life of unconstrained Ni-Mn-Ga single crystals in a rotating magnetic field

Hu Zhang,[1, 2,*] Andrew Armstrong,[2] Peter Müllner[2, *]

[1] *School of Materials Science and Engineering, University of Science and Technology of Beijing, Beijing 100083, P R China.*

[2] *Micron School of Materials Science and Engineering, Boise State University, Boise, ID 83725, USA.*

Abstract

Long-term fatigue life during high-cycle magnetic-mechanical actuation is crucial to the application of Ni-Mn-Ga ferromagnetic shape memory alloys (FSMAs). It has been reported that long fatigue life can be achieved by both reducing surface damage and constraining Ni-Mn-Ga single crystals to exhibit much lower strain than the theoretical limit. In the present study, the fatigue life of Ni-Mn-Ga single crystal samples treated with various surface modifications was investigated in a rotary fatigue testing instrument. The apparatus minimally constrained the samples and allowed for magnetic-field-induced strain (MFIS) close to the theoretical limit. We first treated the samples with electropolishing, which we found created more surface defects than those of the mechanically polished sample. These defects acted as dispersed pinning sites for twin boundaries and nucleated cracks easily due to the localized stress concentration, resulting in reduced fatigue life. We then studied the

*) Corresponding authors

E-mail addresses: zhanghu@ustb.edu.cn (Hu Zhang), petermullner@boisestate.edu (Peter Müllner)

introduction of residual compressive stresses imparted by micropeening. Although micropeening increased surface roughness, it produced a uniform surface morphology and a finely twinned structure. We argue that the distribution of dislocation pile up was more homogeneous due to the fine twin structure, lowering the crack nucleation rate. Consequently, the fatigue life of unconstrained Ni-Mn-Ga single crystals with large MFIS was significantly improved by the micropeening treatment.

Keywords: Ferromagnetic shape memory alloys; Ni_2MnGa; High cycle fatigue; Cracking; Surface treatments.

1. Introduction

Since the discovery of magnetic field-induced strain (MFIS) in ferromagnetic shape memory alloys (FSMAs) with strain greater than obtained in magnetostrictive materials, FSMAs have attracted much attention due to their promising application in actuators and sensors [1-4]. At present, off-stoichiometric Ni_2MnGa FSMAs have been studied intensively because they exhibit high MFIS up to 12% due to a large magnetic anisotropy constant and high magnetic and martensitic transformation temperatures [5-8]. On the microscopic scale, the MFIS is caused by the magnetic-field-induced reorientation of the twin variant structure, in which the short axis (*c*) of the martensite close-to-tetragonal crystal lattice aligns with the magnetic field direction [9-11]. Put another way, the MFIS is a magnetoplastic deformation resulting from twin boundary movement driven by magnetostress [12]. Since the FSMAs are required to undergo long-term cycling of MFIS for practical applications, it is crucial to study the magneto-mechanical fatigue behavior of FSMAs.

The fatigue behavior is closely related to the nucleation of cracks during high-cycle magnetic-mechanical actuation. If the twin boundary motion is obstructed by interacting twins, stresses concentrate at twin boundaries creating a pile-up of twinning dislocations [13, 14]. Thus, cracks nucleate at twin boundaries due to stress concentration and eventually lead to the fracture of FSMAs. Generally, the twin boundaries can move readily in the crystals with thick twins, and large MFIS can be obtained. But cracks also easily nucleate in such crystals, resulting in a short lifetime [15, 16]. In contrast, twin boundaries

cannot move long distances in a sample consisting of many thin twins, since twin boundary movement is strongly hindered by the densely twinned microstructure. Thus, MFIS is relatively smaller and the stress distribution is more homogeneous than that in a coarse twin microstructure. Researchers have suggested that crystals with thin twin structure are more resistant to crack nucleation and so exhibit a longer fatigue life [13, 17].

On the other hand, it is known that the surface defects could act as dispersed pinning sites which hinder the motion of twin boundaries and cause stress concentrations [18, 19]. Therefore, it has been suggested that the twinning stress can be reduced largely by removing the damaged surface layer, which should improve fatigue life considerably [16, 20]. Straka et al. demonstrated enhanced fatigue life for samples with a find twin microstructure, which was stabilized by micropeening the surface [REF]. In addition, macroscopic constraints as an unavoidable component of certain sample holders have also been considered as one of the key factors that affect the MFIS as well as fatigue life [13, 21, 22]. The constraints reduce and even block the movement of twin boundaries, and lead to a remarkable reduction of MFIS [23]. Meanwhile, the fatigue life is shortened in single-domain crystals, because constraints hinder the microstructure from adapting to the internal stress; while a prolonged fatigue life can be achieved in crystals exhibiting self-accommodated multi-domain martensite since the dense twin structure could be stabilized by the constraints [13, 24].

Consequently, it is a challenge to develop such a Ni-Mn-Ga FSMA that shows both large MFIS and long fatigue life. In order to achieve this goal, it is desirable to design a

crystal in which twins are fine but do not obstruct each other [16]. In the present work, the effects of surface modifications on the fatigue life of unconstrained Ni-Mn-Ga single crystals have been studied in detail. The fatigue life was diminished significantly following an electropolishing treatment, which caused pitting and surface non-uniformity. Notably, micropeening gave rise to a fine twin microstructure, leading to a homogeneous stress distribution. Following micropeening, fatigue life was improved remarkably while the MFIS remained large.

2. Experimental

A single crystal with nominal composition $Ni_{50}Mn_{28}Ga_{22}$ was grown using the Bridgman-Stockbarger technique described in detail in Ref. [25]. The growth direction was parallel to $<100>_{austenite}$, and the size of the initial ingot was 6.3 mm in diameter and 75 mm in length. The crystal structure, orientation, and lattice parameters were determined with X-ray diffraction along the length of single crystal using a Bruker D8 diffractometer with Cu Kα radiation. The composition along the length of crystal was investigated using a Hitachi scanning electron microscopy (SEM) with Energy Dispersive Spectroscopy (EDS, Oxford).

Twenty-five disc samples with ~1.4 mm thickness were cut from the 10M portion of crystal along the axial direction using a Princeton Scientific precision wire saw and divided into five groups with five samples in each group (Table 1). After cutting, all samples were electropolished for 20 s in a solution of ethanol and nitric acid (volume ratio 2:1) at 12 V. Both sides of all samples were then mechanically polished using a polishing wheel with

progressive grinding steps from 1200 to 4000 grit SiC paper followed by polishing with water-based diamond suspension from 3 μm to 0.04 μm (group I). Three groups of samples (II, III, IV) were then electropolished for a second time with the same electropolishing parameters while another group (II_{half}) was only submerged halfway into the electropolishing solution during this second electropolishing. Groups III and IV were micropeened with 100 μm SiO_2 particles (Comco) for 8 s under a nozzle pressure of 25 psi (0.17 MPa) on one side and both sides, respectively. Table 1 lists the different groups with different surface treatments. After the surface treatments, all samples were magnetically trained under a magnetic field of 1 T in order to obtain a single variant structure.

A MicroSense Model 10 vibrating sample magnetometer (VSM) was used to determine the austenite transition temperature (A_S) and the switching field of each sample. The samples were initially loaded with the magnetic field parallel to the sample's circular face. The samples were fully magnetized in this orientation in a first isothermal magnetization by increasing the magnetic field up to 1.2 T. Then, the samples were rotated 90° for the second measurement so that the magnetic field was perpendicular to the sample face, and then rotated back to the parallel direction for the third measurement. The switching fields were determined from the second and third measurements of isothermal magnetizations. The *M-H* curves were corrected for the demagnetization effect, i.e., $H_{\text{int}} = H_{ext} - N_d M$, where H_{eff} is the effective field, H_{ext} is external field, and N_d is the demagnetization factor that is determined by the length/diameter ratio [26]. As a result of the demagnetization effect, the slope of the *M*-H_{eff} curve may be negative if the

magnetization increases abruptly with a small increase of the external magnetic field (e.g. in [20]).

Rotary fatigue tests were carried out in a custom-made apparatus, in which the samples were oriented such that the $[010]_S$ was parallel to the axis of rotation and the $[001]_S$ direction was perpendicular to the axis of rotation. The maximum magnetic field parallel and perpendicular to the sample face was 0.52 T and 0.65 T, respectively. The samples were kept in the sample mount by rubber rings, and were thus nearly free of mounting constraints. Details about the rotary fatigue test were given in Ref. [20].

The microstructure was inspected using a Leica DM6000 microscope with differential interference contrast (DIC). The average surface roughness R_a was determined with an optical profilometer (Veeco, WYKO NT110). A custom made optical magneto-mechanical device (OMMD) was set up as shown in Fig. 1(a) in order to record the evolution of twin structure and strain during the rotation of the magnetic field. The sample (1) was attached to the sample holder (2) by double-sided tape. An HD camera (5) recorded the reflection of the sample viewed through a mirror (3) while a sequence-controlled motor rotated the apparatus in the magnetic field (6) of a V3036 electromagnet (Varian Associates). The sample and the camera were rigidly connected and rotated synchronously such that from the sample/camera reference space, the field rotated about the sample. Fig. 1(b) shows an image of a micropeened IV sample for an example. The dash line denotes the orientation of the rotation axis. By analyzing the variation of the diameter r based on the images using software (Imagetool), the magnetic-field-induced strain (MFIS) was measured given $\varepsilon =$

$\frac{r-r_{min}}{r_{min}} \times 100\%$. The relative error $\Delta\varepsilon_{max}/\varepsilon_{max}$ of this method was of the order of 10^{-2}. Furthermore, an open source, MATLAB based 2D DIC software (Ncorr) [27] was used to analyze the evolutionary process of localized strain and twin boundary movement during the rotation of the magnetic field.

3. Results

3.1 Magnetic properties of $Ni_{50}Mn_{28}Ga_{22}$ single crystal

The crystal structure was investigated with XRD, and it was found from Fig. 2 that the sample formed the10M martensite structure at the seed end and then exhibited 14M martensite after 54 mm. The disc samples were cut from the 10M section of the single crystal. The composition along the axis of the crystal was analyzed by EDS and is shown in Fig. 2(a). The actual composition of different elements was nearly consistent with the nominal composition $Ni_{50}Mn_{28}Ga_{22}$. Howeverr, the Mn concentration increased while the Ni and Ga contents decreased slightly along the growth direction. The austenite starting temperatures (A_S) of different samples were determined by thermomagnetic curves in a low field (0.025 T), and are also summarized in Fig. 2(a). The A_S increased gradually along the growth direction. Figure 2(b) shows the A_S as a function of Mn concentration. The A_S increased with the increase of Mn concentration, which is consistent with previous reports [28, 29]. In addition, the A_S of all samples was higher than the room temperature of our laboratory (22 ℃), suggesting that all samples were in the martensite state during the fatigue experiments.

The isothermal magnetization was measured to investigate the switching field and Fig. 3 shows the isothermal magnetization of an I sample with the magnetic field parallel and perpendicular to the sample face respectively. The magnetization curves show a distinct difference between the different directions, which is due in part to the large difference of demagnetizing fields along different directions [20]. In addition, the effective field H_{eff} decreased due to the twin switching process, which causes the sharp increase of M . Thus a higher magnetization can be obtained at lower effective field when the easy axis switches to the direction of the magnetic field. The effective switching fields, determined based on the isothermal magnetizations after demagnetization correction, were 0.27 T and 0.10 T for field parallel and perpendicular to the face, respectively, which were lower than the maximum field supplied by our rotary fatigue testing instrument along parallel (0.52 T) and perpendicular (0.65 T) directions [20]. Moreover, the switching fields of all samples were lower than the maximum field of the rotary fatigue testing instrument, implying full realization of periodic, reversible magnetic-field-induced strain (MFIS) of all samples in the testing instrument.

3.2 Effects of electropolishing on fatigue life

Figure 4(a) displays the mosaic DIC optical micrograph of the sample with treatments I (mechanically polished finish) and II (electropolished finish) on each half of the sample. The half with treatment I had a very smooth surface, while the other half with treatment II was much rougher with many corrosion pits caused by the electropolishing (Fig. 4 (b)). Figures 4(c) and 4(d) show the micrographs taken with an optical profilometer for each

half of the sample. The average surface roughness R_a was 7.99 nm and 38.74 nm for the half with treatments I and II, respectively. Thus, the electropolishing treatment increased the surface roughness compared to mechanical polishing.

Initially, the MFIS was investigated for a I sample and a II sample. Fig. 5 shows the MFIS as a function of field rotation angle under different magnetic fields for I and II treated samples. At zero degrees of rotation, the magnetic field was perpendicular to the sample face, leading to the orientation of short *c* direction perpendicular to the sample face and the long *a* direction along the radial direction and, thus, the largest MFIS. The MFIS varied periodically with the rotation of the magnetic field due to the reorientation of variants, and it increased with increasing magnetic field. The large strain under low fields at the initial angle was artificial, likely caused by pressing the sample into the mounting tape of the holder.

Figure 6 presents the DIC optical micrograph of the sample with treatment I on one half and treatment II on the other half of the sample after 1,000 cycles of rotary fatigue testing. The half with treatment I kept good integrity (i.e. few cracks are visible). In contrast, the half with II treatment showed large cracks after 1,000 cycles, indicating that the electropolishing treatment diminished the fatigue life. Meanwhile, as shown in Fig. 6(b), these cracks zigzag back and forth horizontally in <110> directions across the face, consistent with previous studies [20, 24].

3.3 Effects of micropeening on fatigue life

Figure 7 shows the bulk XRD spectra of II (electropolished finish) and IV (micropeened finish) samples at 100°C. In order to avoid the possible difference induced by the different orientations of tetragonal martensite, the XRD patterns were obtained with the sample in cubic austenite state by heating the samples to 100°C. Both samples showed a diffraction peak (400) of austenite at 63.7°, but the full width at half maximum (FWHM) increased from 0.48° for the non-micropeened sample to 3.20° for the micropeened sample. The micropeening treatment thus introduced strain on the surface of the sample, causing broadening of the diffraction peak.

Figures 8(a) and 8(b) compare the mosaic DIC optical micrographs of the non-micropeened sample (II) and micropeened sample (IV). The II sample (Fig. 8(a)) showed a rough surface with corrosion pits which were caused by electropolishing., Twin boundaries were visually apparent on the surface of II sample. In contrast, the IV sample showed a uniform frosted-like surface and the twin boundaries were not visually apparent. The topography images of II and IV samples from the optical profilometer are presented in Figs. 8(c) and 8(d). The II sample showed clear twin boundaries with a surface R_a of 90.18 nm. For the IV sample, no twin boundaries were visible, and the surface R_a was 315.06 nm. Although the R_a was higher after micropeening, the surface morphology was uniform. Figure 9 shows the isothermal magnetizations after demagnetization correction for II, III, and IV samples, respectively. There is no distinct difference of the *M-H* curves between II and III samples. However, the increase in magnetization due to the reorientation of variants

was smooth for the IV sample, and thus twin domain switching occurred over a range of the magnetic field, consistent with fine-twin-controlled MFIS [14].

Figures 10 presents the MFIS as a function of field rotation angle under different magnetic fields for II, III, and IV samples, respectively. The II sample exhibited the full MFIS, the strain plateauing at 0.52 T, similar to the results of previous reports [22, 30]. The MFIS decreased slightly in III and IV samples after the micropeening treatment and exhibited a less broad plateau. The magnetic field dependence of the maximum MFIS is plotted in Fig. 10(d). No samples, regardless of treatement exhibited MFIS below 0.1 T, indicating that the switching field of all samples was higher than 0.1 T. The II sample began to exhibit MFIS of ~3.0% under a magnetic field of 0.2 T, while MFIS under 0.2 T was lower in III (about 1%) and IV (below 0.5%) samples, suggesting a reduction of twin boundary mobility at low field strength. In addition, the maximum MFIS under 0.52 T was 6.35%, 5.41%, and 4.98% for II, III, and IV samples, respectively. The micropeening treatment appeared to sligihtly hamper twin boundary movement, leading to an increase in switching field as well as a slight reduction in overall MFIS.

The mosaic DIC optical micrographs of the II, III, and IV samples after rotary fatigue tests are presented in Fig. 11. The II sample failed after 1,000 cycles, exhibiting large cracks, consistent with results shown in Fig. 6. With the micropeening treatment on one side, the III sample exhibited a much longer fatigue life, but broke into several sections after 12,000 cycles. A fine twin microstructure was visibly apparent on the non-micropeened side of III sample, as shown in Fig. 11(b), but these twins were not discernable on the micropeened

side (Fig. 11(d)). The IV sample with micropeening on both sides maintained excellent integrity without exhibiting obvious cracks even after 1,000,000 cycles as shown in Fig. 11(c). The micropeening treatment significantly improved the fatigue life of the FSMA three orders of magnitude.

In order to further study the effect of rotary fatigue test on the microstructure evolution of IV sample, one IV sample before the fatigue test and one following the fatigue test was sectioned in half, and the microstructure of their cross sections was investigated with DIC as shown in Fig. 12. The IV sample showed a single twin variant microstructure without twin boundaries or any other defects before the fatigue cycling. After 1,000,000 cycles, small cracks along <011> direction appeared, propogating from the circumference.

Figure 13 shows the isothermal magnetizations of IV samples after 500,000 and 1,000,000 cycles, respectively. In comparison with the isothermal magnetizations of the sample before cycling in Fig. 9(c), the *M*-*H* curves become much smoother yet demonstrated clear domain switching along the parallel direction after fatigue testing. Moreover, the *M*-*H* curves after 500,000 and 1,000,000 cycles fully overlap with each other, revealing that the IV sample almost exactly maintained its magnetomechanical properties. The effect of magnetic field cycling on MFIS was evaluated and Fig. 14(a) presents the MFIS as a function of field rotation angle for IV sample after 1, 100,000, and 1,000,000 cycles, respectively. The MFIS curves remained nearly the same but the maximum MFIS decreased slightly with the increasing number of cycles. The cycle dependence of the maximum MFIS is plotted in Fig. 14(b). The maximum strain declined quickly from 4.98%

for the first cycle to 4.49% after 100,000 cycles, and then decreased more gradually. Although the MFIS decreased slightly after the magnetic field cycling, the maximum strain remained relatively high at 4.16% under a modest field of 0.52 T after 1,000,000 cycles.

To further investigate the evolutionary process of local strain and twin boundaries during the rotating-field test, a series of DIC images with rotation step of 5° were analyzed with an open source, MATLAB based 2D DIC software Ncorr [27]. Figure 15 shows the in-plane Green-Lagrangian strain component ε_{yy} derived from Ncorr for a series of DIC images of micropeened IV sample with an angular resolution of 15° and spatial resolution of 0.008 mm/pixel. The magnetic field was perpendicular to the sample face at 0°, and the rotation axis was along the X axis. Therefore, the twin boundaries moved along the Y axis, and lead to MFIS in this direction. The DIC image at 90° was chosen as the reference image since the short axis (*c*) was along the Y axis at 90°. The angle was then reduced to 0°. The crystal did not show obvious strain above 45°, but distinct strain appeared immediately following and increased with further rotation, reaching the maximum at 0°.

4. Discussion

During magnetic field actuation, twin boundaries move through the crystal driven by magnetostress. If the sample is constrained by the holder, the motion of twin boundaries is restricted at the sample ends if these are adhered to and constrained by the sample holder, which leads to a large reduction of MFIS [23]. Moreover, a stress concentration develops at the sample ends from the increase in magneto-mechanical response, nucleating cracks and eventually causing fracture if the twins are thick [15, 17]. In the present work, the Ni-

Mn-Ga single crystal disk was not constrained during the rotating-field testing, and it shows a large MFIS of up to 6.35%, much higher than the (1~2%) in experiments with constrained samples that previously showed good fatigue performance [23].

Surface defects hinder the motion of twin boundaries, leading to stress concentrations and nucleating cracks [16, 19]. Electropolishing has thus been suggested as an effective way to prevent damage accumulation in Ni-Mn-Ga FSMA crystals during high-cycle magnetic-mechanical actuation as it reduces surface defects and decreases twinning stress [13]. In contrast, in our study the electropolishing caused much more damage on the surface compared to mechanically polishing with 0.04 μm water-based diamond suspension as shown in Fig. 4, and the electropolishing was detrimental to fatigue life. Figure 16 shows a schematic illustrating the effects of surface modification on twin boundary mobility. The I sample exhibits a smooth surface with R_a = 7.99 nm after mechanical polishing with 0.04 μm diamond suspension. The twinning stress is low, and the twin boundaries move smoothly through the entire crystal without pinning from surface defects (Fig. 16(a)) [31]. The twin boundary motion is obstructed by a few coarsely dispersed internal obstacles and defects (schematically illustrated by the blue object in the center of Fig. 16(a)). In comparison, electropolishing creates a rougher surface with a number of corrosion pits, which act as dispersed pinning sites for twin boundaries as shown in Fig. 16(b). Cracks nucleate easily at these pinning sites due to stress concentration, significantly reducing the fatigue life [20]. In addition, cracks propagate along 45° with the edges of sample in all surfaces, e.g., the cracks progress zig-zagging back and forth horizontally in <110>

directions on the top surface, and develop along <011> direction on the cross section. Thus the cracks preferentially propagate along the {111} crystal planes, which is in a good agreement with previous studies [20, 24].

Although the micropeening increases surface roughness, the surface morphology is uniform compared with the electropolished sample (Fig. 8). The homogeneously distributed defects provide homogeneous pinning sites for twin boundaries, creating numerous small and thin twins as described in Fig. 16(c). This dense twin microstructure is visible in the non-micropeened side of III sample in Fig. 11(b). Moreover, since these small twins were decomposed from a well-trained single variant, the orientation of these small twins should be very close, explaining why the twin boundaries cannot be observed clearly using optical methods on the micropeened surface (Fig. 8(b) and Fig. 11(c)). Similar to the effect of ineffective training described in Ref. [17], twin boundary mobility is somewhat inhibited in the micropeened crystals with densely twinned microstructure, and the MFIS becomes lower after micropeening. However, whilemany dislocations pile-up at defects and nucleate cracks in the non-micropeened crystal with coarse twins, in the micropeened sample with a fine twin structure [15] pile-ups of dislocations are small and more homogeneously distributed. Therefore, the fatigue life during the high-cycle magneto-mechanical tests is significantly improved by micropeening.

In electropolished samples with low defect density, twin boundaries typically move through the entire samples [32]. When starting in a single domain crystal, the twinning stress and the switching field are mainly controlled by the nucleation of twin boundaries.

Thus, the twinning stress starts out high (above 1 MPa) and quickly drops to below 0.5 MPa, following the nucleation of a twin boundary. This results in an abrupt switching field. In contrast, if twin boundaries are already present, the nucleation energy is irrelevant, and the twinning stress is below 0.5 MPa, and thus switching begins at a lower magnetic field. Further, the density of twins impacts the twinning stress and stress evolution [33]. For a crystal with only one twin boundary, the twinning stress can be low (0.1 MPa for type II twins) and constant over the entire deformation range covered by twin boundary motion. In contrast, for a crystal with a high density of parallel twin boundaries, the twinning stress begins at about 0.3 MPa and increases monotonically until twin deformation saturates, inhibited by adjacent pinned twin boundaries. The effect of micropeening on the switching field can therefore be explained as in the electropolished state, switching occurs abruptly when a twin boundary is nucleated and then propogates through the sample (Fig. 9(a)). But in the micropeened state, many twins are present and pinned by the surface defects. The twin boundaries can move partially within the crystal at a very low twinning stress, and thus at a small magnetic field. However, the magnetostress must counter the pinning force of the surface defects introduced by micropeening to complete switching. Therefore, switching starts at a low magnetic field and gradually proceeds with increasing magnetic field to complete at a rather high magnetic field (Fig. 9(c)).

The evolutionary process of twinning is also evident when comparing the strain maps obtained from Ncorr software (Fig. 15) with the rotation degree dependence of MFIS shown in Fig. 10. The regions where the twin boundaries have moved is given by the ε_{yy}

contours. The transition between blue (small strain) and red (large strain) implies that twin density is high (Fig. 11), such that the twin boundaries are not well resolved with the Ncorr strain analysis. The Ncorr software analyzes the strain average over an area larger than the twin width. In areas where the twin boundaries overcome the pinning forces, the ε_{yy} strain component is large. It appears that twin boundaries overcome pinning forces locally, followed by growth of the strained regions. In addition, the component of magnetic field along the radial direction is greater than that along the axial direction when the angle is above 45°. This indicates why the crystal does not show a strain above 45°, and then distinct strain appears and grows with further rotation, which reaches maximum at 0°. (Fig. 15 and supplementary video).

5. Conclusions

The effects of surface electropolishing and micropeening treatments on the fatigue life of unconstrained $Ni_{50}Mn_{28}Ga_{22}$ single crystals in a rotating magnetic field were systematically studied. In comparison with the mechanically polished sample with 0.04 μm water-based diamond suspension, electropolishing increases the surface roughness, creating coarsely dispersed pinning sites for twin boundaries. Subsequently, the fatigue life is diminished significantly because the twinning dislocations easily pile up at the pinning sites and then nucleate cracks due to the stress concentration. Conversely, the micropeening treatment produces a uniform surface morphology with a dense distribution of small defects which stabilize a very fine twin structure. The homogeneously distributed surface defects provide homogeneous pinning sites for twin boundaries, which hinder the twin

boundary motion, leading to the slight reduction of MFIS. However, large groups of dislocations do not pile up as in the electropolished sample and the stress distribution is more homogeneous due to the fine twin structure in the micropeened sample. The fatigue life is thus remarkably improved by the micropeening treatment. The present work indicates that fatigue life is not only related to the surface defects but also affected by the twin microstructure. Micropeening that produces homogeneous surface morphology as well as fine twin microstructure appears to be an effective method to improve fatigue life while maintaining a large MFIS.

Acknowledgements

The authors thank Justina Freilich for assistance with single crystal growth and DIC microscopy, Brent Johnston for making the sample holder for the OMMD, and Dr. Aaron Smith, Dr. Tony Hobza, and Dr. Paul Lindquist for fruitful discussions. This work was supported by the National Natural Science Foundation of China (Grant No.: 51671022); the National Key Research and Development Program of China (Grant No.: 2017YFB0702704); the Beijing Natural Science Foundation (No. 2162022); and the China Scholarship Council (No. 201606465010). PM and AA acknowledge partial financial support from the National Science Foundation through projects NSF IIP-1500240 and NSF DMR-1710640 and an equipment donation (V3603 electromagnet) by NanoSteel, Idaho Falls, Idaho.

References:

[1] M. Chmielus, X. X. Zhang, C. Witherspoon, D. C. Dunand, P. Müllner, Giant magnetic-field-induced strains in polycrystalline Ni-Mn-Ga foams, Nat. Mater. 8 (2009) 863.

[2] D. C. Dunand, P. Müllner, Size effects on magnetic actuation in Ni-Mn-Ga shape-memory alloys, Adv. Mater. 23 (2011) 216.

[3] I. Suorsa, J. Tellinen, E. Pagounis, I. Aaltio, K. Ullakko, Applications of magnetic shape memory alloys, Proceedings of the 8th International Conference on Actuators, Bremen, Germany, 10-20 June 2002, p. 158.

[4] P. Müllner, V. A. Chernenko, G. Kostorz, Stress-induced twin rearrangement resulting in change of magnetization in a Ni-Mn-Ga ferromagnetic martensite, Scr. Mater. 49 (2003) 129.

[5] K. Ullakko, J. K. Huang, C. Kantner, R. C. O'Handley, V. V. Kokorin, Large magnetic-field-induced strains in Ni_2MnGa single crystals, Appl. Phys. Lett. 69 (1996) 1966.

[6] A. Sozinov, A. A. Likhachev, N. Lanska, K. Ullakko, Giant magnetic-field-induced strain in NiMnGa seven-layered martensitic phase, Appl. Phys. Lett. 80 (2002) 1746.

[7] J. M. Guldbakke, M. Chmielus, K. Rolfs, R. Schneider, P. Müllner, A. Raatz, Magnetic, mechanical and fatigue properties of a $Ni_{45.4}Mn_{29.1}Ga_{21.6}Fe_{3.9}$ single crystal, Scr. Mater. 62 (2010) 875.

[8] A. Sozinov, N. Lanska, A. Soroka, W. Zou, 12% magnetic field-induced strain in Ni-Mn-Ga-based non-modulated martensite, Appl. Phys. Lett. 102 (2013) 021902.

[9] R. C. O'Handley and S. M. Allen, Shape memory alloys, magnetically activated ferromagnetic shape-memory materials, *Encyclopedia of Smart Materials*, ed M. Schwartz (New York: Wiley) 2002, p. 936.

[10] O. Söderberg, Y. Ge, A. Sozinov, S.-P. Hannula, V. K. Lindroos, *Handbook of Magnetic Materials*. ed J. Buschow (Amsterdam: Elsevier) 2006, p. 1.

[11] I. Aaltio, O. Heczko, O. Söderberg, S.-P. Hannula, *Smart Materials*, ed M. Schwartz (CRC Press, Boca Raton, FL) 2009, p. 20.

[12] P. Müllner, V. A. Chernenko, M. Wollgarten, G. Kostorz, Large cyclic deformation of a Ni-Mn-Ga shape memory alloy induced by magnetic fields, J. Appl. Phys. 92 (2002) 6708.

[13] M. Chmielus, P. Müllner, Effects of surface pinning, locking, and adaption of twins on the performance of magnetic shape-memory alloys, Mater. Sci. Forum 684 (2011) 177.

[14] P. Müllner, G. Kostorz, Microstructure of magnetic shape-memory alloys: between magnetoelasticity and magnetoplasticity, Mater. Sci. Forum 583 (2008) 43.

[15] P. Müllner, V. A. Chernenko, D. Mukherji, G. Kostorz, Cyclic magnetic-field-induced deformation and magneto-mechanical fatigue of Ni-Mn-Ga ferromagnetic martensites, Mater. Res. Soc. Symp. Proc. 785 (2004) 415.

[16] M. Chmielus, C. Witherspoon, K. Ullakko, P. Müllner, R. Schneider, Effects of surface damage on twinning stress and the stability of twin microstructures of magnetic shape memory alloys, Acta Mater. 59 (2011) 2948.

[17] M. Chmielus, V. A. Chernenko, W. B. Knowlton, G. Kostorz, P. Müllner, Training, constraints, and high-cycle magneto-mechanical properties of Ni-Mn-Ga magnetic shape-memory alloys, Eur. Phys. J. Special Topics 158 (2008) 79.

[18] L. Straka, O. Heczko, H. Hänninen, Activation of magnetic shape memory effect in Ni-Mn-Ga alloys by mechanical and magnetic treatment, Acta Mater. 56 (2008) 5492.

[19] M. Chmielus, K. Rolfs, R. Wimpory, W. Reimers, P. Müllner, R. Schneider, Effects of surface roughness and training on the twinning stress of Ni-Mn-Ga single crystals, Acta Mater. 58 (2010) 3952.

[20] T. Lawrence, P. Lindquist, K. Ullakko, P. Müllner, Fatigue life and fracture mechanics of unconstrained Ni-Mn-Ga single crystals in a rotating magnetic field, Mater. Sci. Eng. A 654 (2016) 221.

[21] C. P. Henry, D. Bono, J. Feuchtwanger, S. M. Allen, R. C. O'Handley, as field-induced actuation of single crystal Ni-Mn-Ga, J. Appl. Phys. 91 (2002) 7810.

[22] P. Müllner, V. A. Chernenko, G. Kostorz, Large cyclic magnetic-field-induced deformation in orthorhombic (14M) Ni-Mn-Ga martensite, J. Appl. Phys. 95 (2004) 1531.

[23] M. Chmielus, I. Glavatskyy, J.-U. Hoffmann, V. A. Chernenko, R. Schneider, P. Müllner, Influence of constraints and twinning stress on magnetic field-induced strain of magnetic shape-memory alloys, Scr. Mater. 64 (2011) 888.

[24] I. Aaltio, A. Soroka, Y. Ge, O. Söderberg, S. P. Hannula, High-cycle fatigue of 10M Ni-Mn-Ga magnetic shape memory alloy in reversed mechanical loading, Smart Mater. Struct. 19 (2010) 075014.

[25] D. Kellis, A. Smith, K. Ullakko, P. Müllner, Oriented single crystals of Ni-Mn-Ga with very low switching field, J. Cryst. Growth 359 (2012) 64.

[26] D. X. Chen, J. A. Brug, Demagnetizing factors for cylinders, IEEE T. Magn. 27 (1991) 3601.

[27] J. Blaber, B. Adair, A. Antoniou, Ncorr: open-source 2D digital image correlation matlab software, Exp. Mech. 55 (2015) 1105.

[28] V. A. Chernenko, E. Cesari, V. V. Kokorin, I. N. Vitenko, The development of new ferromagnetic shape memory alloys in Ni-Mn-Ga system, Scr. Met. Materi. 33 (1995) 1239.

[29] S. K. Wu, S. T. Yang, Effect of composition on transformation temperatures of Ni-Mn-Ga shape memory alloys, Mater. Lett. 57 (2003) 4291.

[30] P. Müllner, V. A. Chernenko, G. Kostorz, Large magnetic-field-induced deformation and magneto-mechanical fatigue of ferromagnetic Ni-Mn-Ga martensites, Mater. Sci. Eng. A 387 (2004) 965.

[31] I. Aaltio, X. W. Liu, M. Valden, K. Lahtonen, O. Söderberg, Y. Ge, S. P. Hannula, Nanoscale surface properties of a Ni-Mn-Ga 10M magnetic shape memory alloy, J. Alloy. Compd. 577 (2013) S367.

[32] I. Aaltio, O. Söderberg, Y. L. Ge, S. P. Hannula, Twin boundary nucleation and motion in Ni-Mn-Ga magnetic shape memory material with a low twinning stress, Scr. Mater. 62 (2010) 9.

[33] L. Straka, N. Lanska, K. Ullakko, A. Sozinov, Twin microstructure dependent mechanical response in Ni-Mn-Ga single crystals, Appl. Phys. Lett. 96 (2010) 131903.

Table 1, Sample groups with different surface treatments. Each group has five disc samples with ~1.4 mm thickness.

Surface treatment \ Group	I	II	II_{half}	III	IV
First electropolishing (volume ratio of ethanol and nitric acid is 2:1, 12 V, 20 s)	√	√	√	√	√
Mechanical polishing (0.04 μm)	√	√	√	√	√
Second electropolishing (volume ratio of ethanol and nitric acid is 2:1, 12 V, 20 s)		√	√ (half sample)	√	√
One-side micropeening (~100 μm powder, 8 s, nozzle pressure: 25 psi)				√	√
Two-side micropeening (~100 μm powder, 8 s, nozzle pressure: 25 psi)					√

Figure captions

Fig. 1. (a) Schematic of the custom made optical magneto-mechanical device (OMMD) for rotary magnetic-mechanical experiment. The sample (1) was attached to the sample holder (2) by double-sided tape, and then the HD camera (5) recorded the reflection of sample through a mirror (3) while these components were rotated in the magnetic field (6) by a sequence-controlled motor. (b) The image of micropeened IV sample as an example; the dashed line marks the rotation axis and the blue line indicates the diameter which was measured to determine the MFIS; both lines were parallel to <100>.

Fig. 2. (a) Actual composition and the austenite starting temperatures (A_S) along the axis of the crystal with 10M structure. Twenty-five disc samples with ~1.4 mm thickness were cut from the 10M portion of crystal along the axial direction as shown at the bottom. (b) Austenite starting temperatures A_S as a function of Mn concentration.

Fig. 3. Isothermal magnetizations of I sample (mechanically polished) with field parallel and perpendicular to the sample face. The switching field is the critical field at which the magnetization jumps. Results are shown with and without demagnetization correction.

Fig. 4. (a) Mosaic DIC optical micrograph of the sample with I (mechanically polished) and II (electropolished) treatments on each half of the sample, and (b) the enlarged image of the square area. The micrographs with an optical profilometer for (c) the half with I treatment and (d) the other half with II treatment, respectively.

Fig. 5. The MFIS as a function of field rotation angle under different magnetic fields for (a) I sample (mechanically polished) and (b) II sample (electropolished). The large strain

under low fields at zero angle as shown in the encircled area is artificially caused by the pressing stress during mounting the sample onto the holder.

Fig. 6. (a) DIC optical micrograph of the sample with I (mechanically polished) and II (electropolished) treatments on each half of the sample after 1,000 field cycles of rotary fatigue test, and (b) the enlarged image of the square area.

Fig. 7. Bulk XRD spectra of non-micropeened (II) and micropeened sample (IV) samples at 100°C around the diffraction peak (400) of austenite at 63.7°.

Fig. 8. Mosaic DIC optical micrographs of the (a) non-micropeened sample (II) and (b) micropeened sample (IV), and the topography images of (c) II and (d) IV samples with an optical profilometer, respectively.

Fig. 9. Isothermal magnetizations with demagnetization correction with field parallel and perpendicular to the sample face for (a) II, (b) III, and (c) IV samples, respectively.

Fig. 10. The MFIS as a function of field rotation angle under different magnetic fields for (a) II, (b) III, and (c) IV samples, respectively. (d) Magnetic field dependence of the maximum MFIS.

Fig. 11. Mosaic DIC optical micrographs of the (a) II sample after 1,000 cycles, (b and d) III sample after 12,000 cycles, and (c) IV sample after 1,000,000 cycles, respectively. (b) non-micropeened side of III sample and (d) micropeened side of III sample.

Fig. 12. Microstructure of the cross sections for IV samples before and after 1,000,000 field cycles of rotary fatigue test.

Fig. 13. Isothermal magnetizations of IV samples with field parallel and perpendicular to the sample face after 500,000 and 1,000,000 cycles, respectively.

Fig. 14. (a) MFIS as a function of field rotation angle under magnetic field of 0.52 T for IV sample after 1, 100,000, and 1,000,000 cycles, respectively. (b) The cycle dependence of the maximum MFIS under 0.52 T for IV sample.

Fig. 15. In-plane Green-Lagrangian strain component ε_{yy} for a series of DIC images of micropeened IV sample with step of 15° derived from Ncorr. The magnetic field is parallel to the sample surface at 90° and the rotation axis is along X axis. The twin boundaries move along Y axis, and lead to the MFIS in this direction. The DIC image at 90° was chosen as the reference image since the short axis (*c*) is along Y axis at 90°.

Fig. 16. Schematic illustrating the effects of surface modification on the twin boundary mobility. The surface conditions correspond to (a) mechanical polished with 0.04 μm diamond suspension, (b) electropolished, and (c) micropeened surfaces. The dark part is the reoriented twin with preferred orientation relative to the external magnetic field. The solid line indicates the twin boundary and the dash lines correspond to the twin boundary arrests during the rotary magnetic-mechanical experiment. The surface defects act as pinning sites for twin boundaries. The twin boundary motion might be obstructed by a few coarsely dispersed internal obstacles and defects in (a), while it would be mainly hindered due to the pinning effect from surface defects in (b) and (c).

Figures

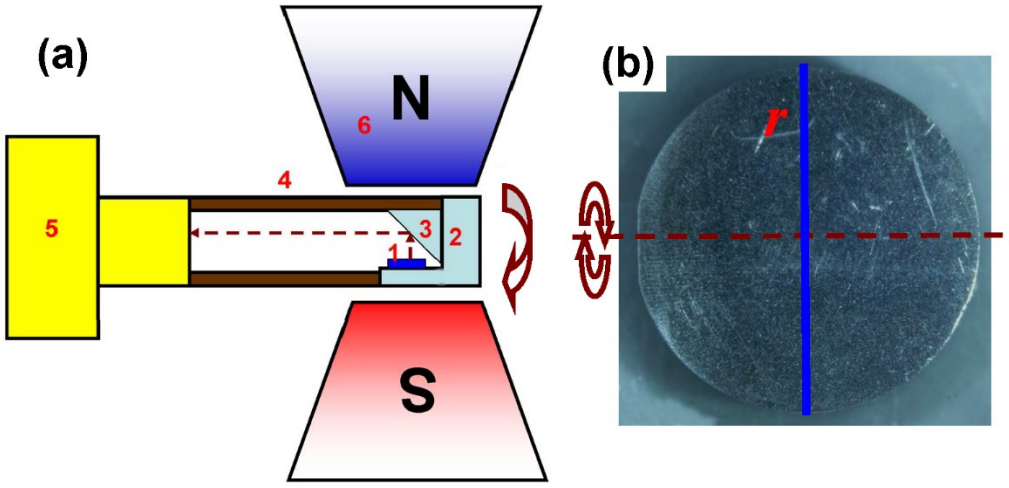

Fig. 1.

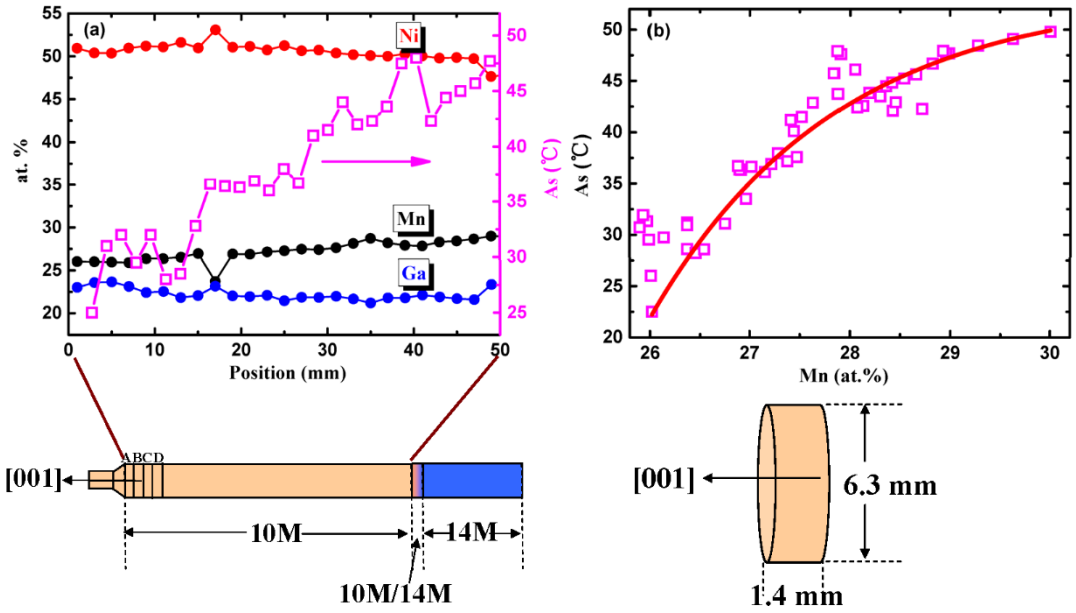
(a)
Ni
Mn
Ga
at. %
As (℃)
Position (mm)
ABCD
[001]
10M
14M
10M/14M
(b)
As (℃)
Mn (at.%)
[001]
6.3 mm
1.4 mm

Fig. 2.

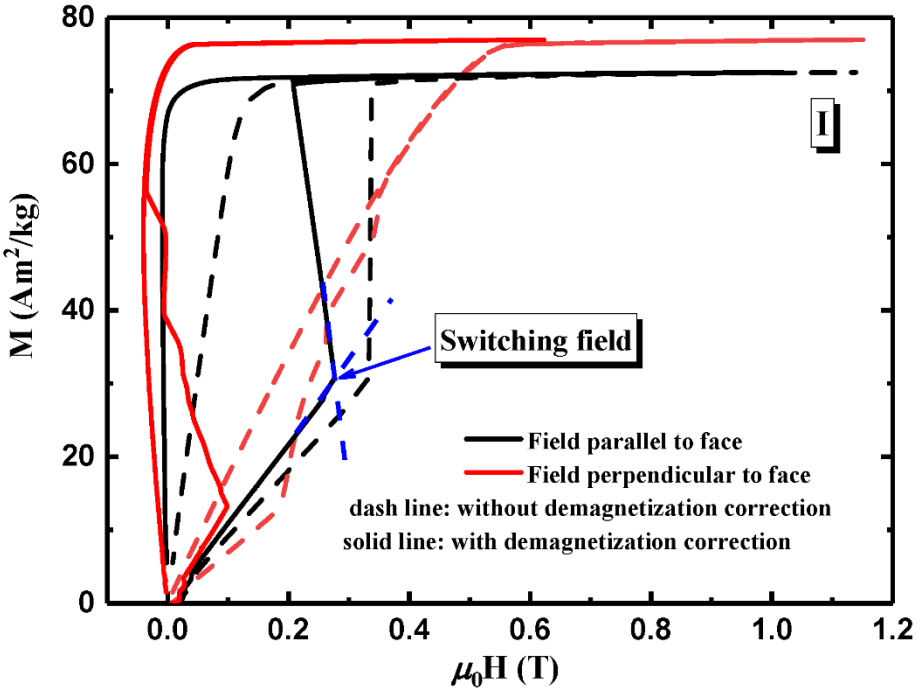
80
60
40
20
0
M (Am²/kg)
0.0
0.2
0.4
0.6
0.8
1.0
1.2
μ0H (T)
I
Switching field
Field parallel to face
Field perpendicular to face
dash line: without demagnetization correction
solid line: with demagnetization correction

Fig. 3.

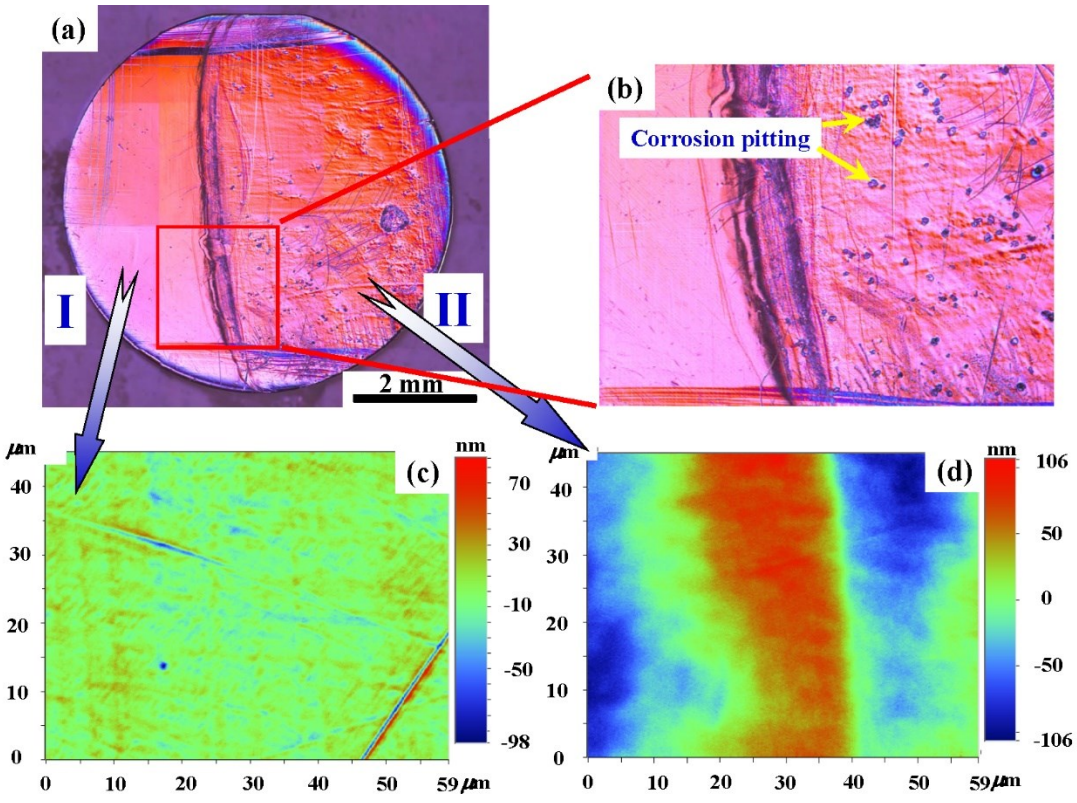
(a)
I
II
2 mm
(b)
Corrosion pitting
(c)
(d)
μm
nm
70
30
-10
-50
-98
106
50
0
-50
-106
0
10
20
30
40
50
59 μm

Fig. 4.

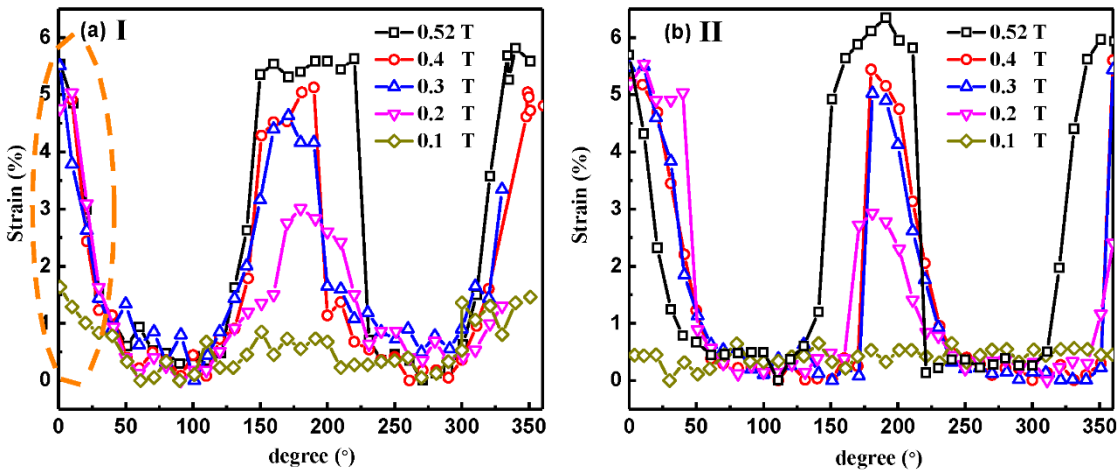
(a) I
(b) II
0.52 T
0.4 T
0.3 T
0.2 T
0.1 T
Strain (%)
degree (°)
0
1
2
3
4
5
6
0
50
100
150
200
250
300
350

Fig. 5.

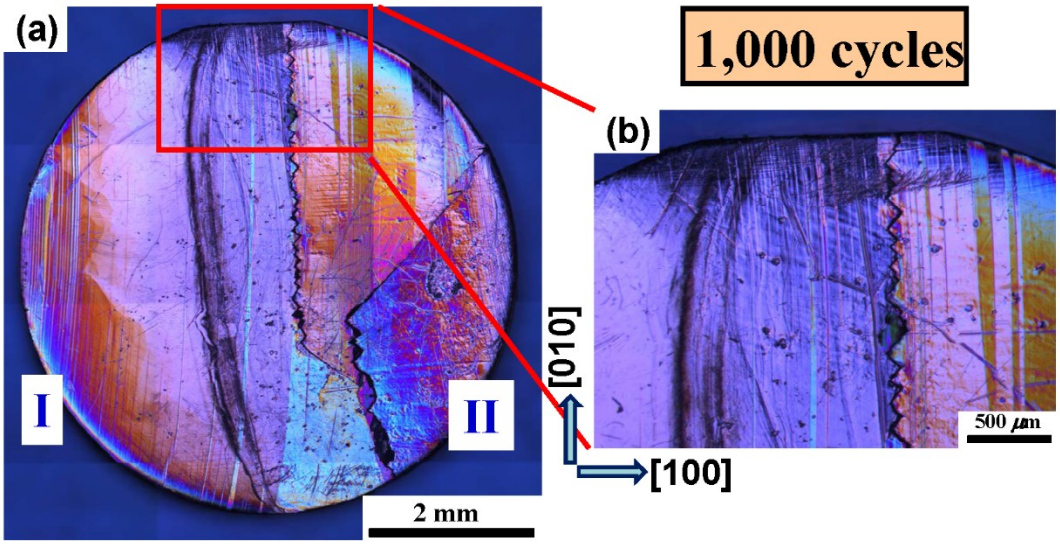

Fig. 6.

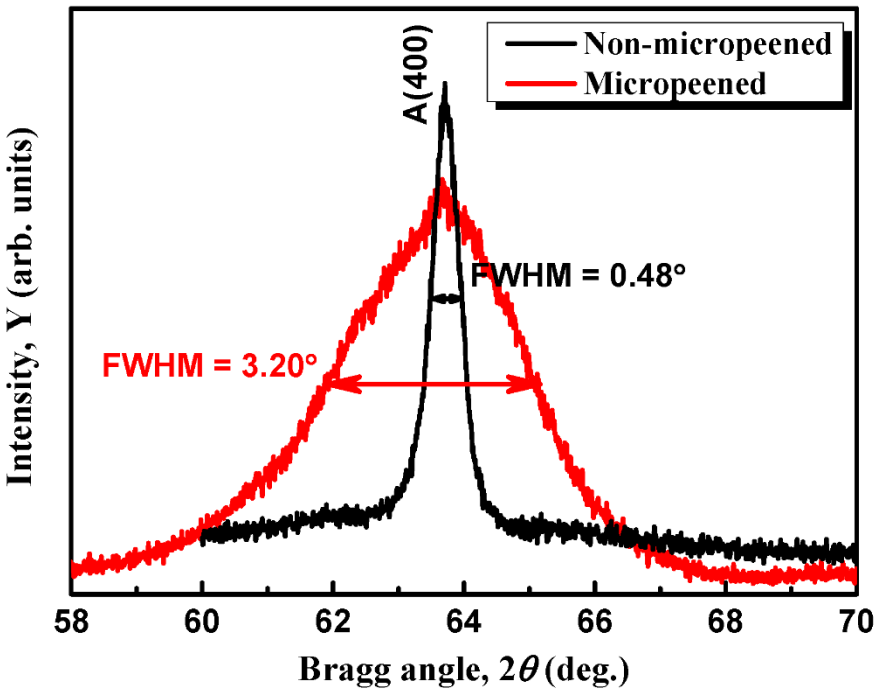
Non-micropeened
Micropeened
A(400)
FWHM = 0.48°
FWHM = 3.20°
Intensity, Y (arb. units)
58
60
62
64
66
68
70
Bragg angle, 2θ (deg.)

Fig. 7.

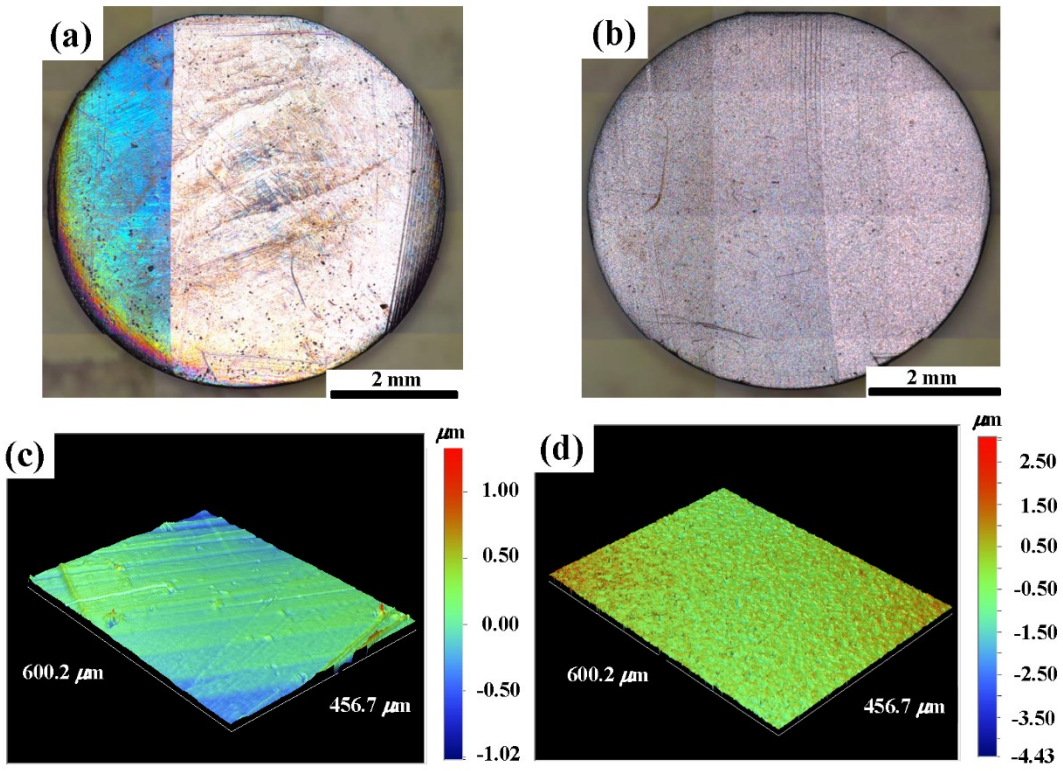
(a)
2 mm
(b)
2 mm
(c)
600.2 μm
456.7 μm
μm
1.00
0.50
0.00
-0.50
-1.02
(d)
600.2 μm
456.7 μm
μm
2.50
1.50
0.50
-0.50
-1.50
-2.50
-3.50
-4.43

Fig. 8.

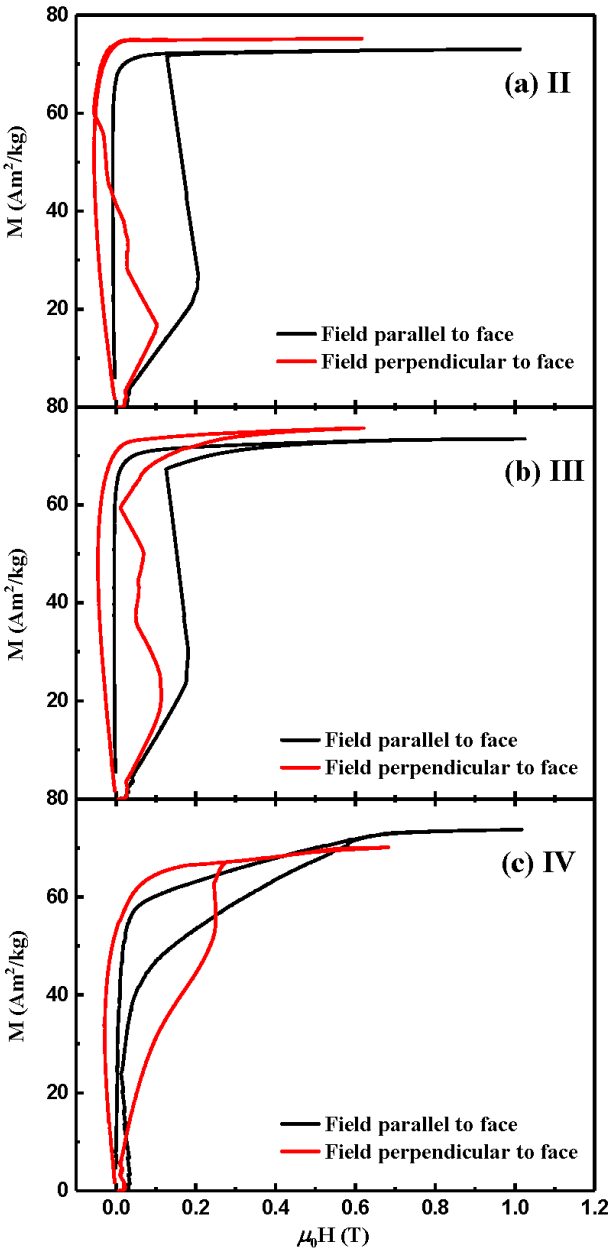
(a) II
(b) III
(c) IV
M (Am²/kg)
Field parallel to face
Field perpendicular to face
μ₀H (T)
80
60
40
20
0
0.0
0.2
0.4
0.6
0.8
1.0
1.2

Fig. 9.

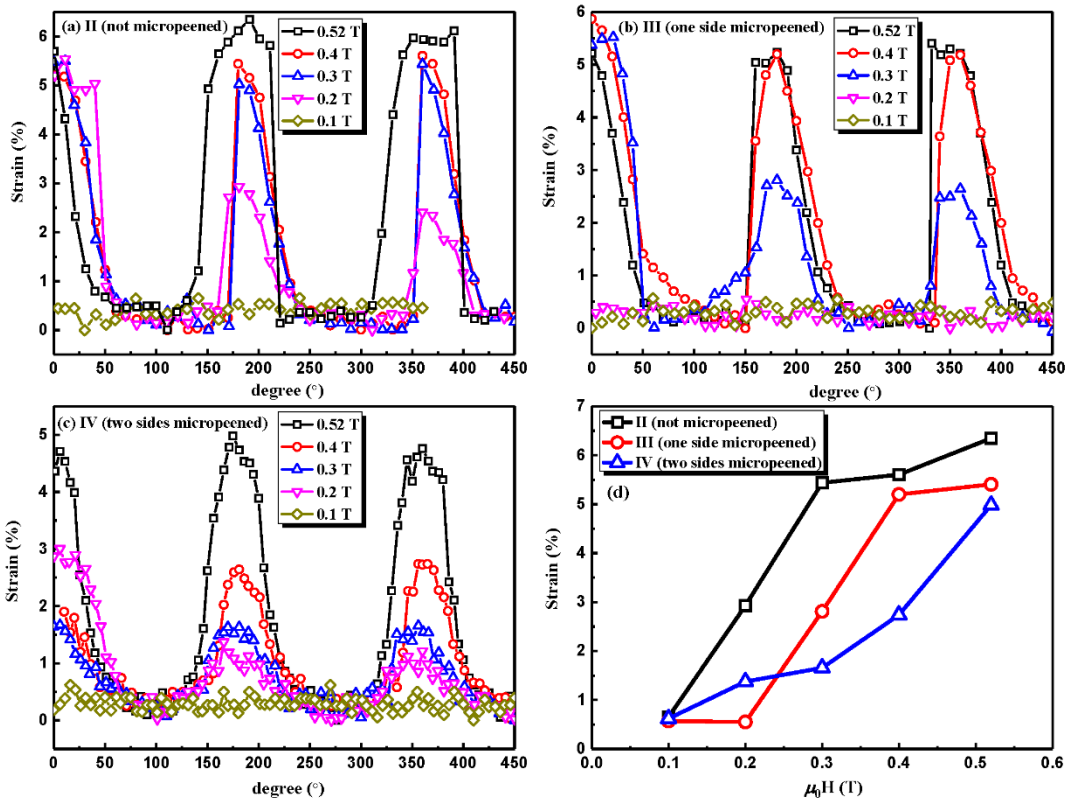
(a) II (not micropeened)
(b) III (one side micropeened)
(c) IV (two sides micropeened)
(d)
0.52 T
0.4 T
0.3 T
0.2 T
0.1 T
Strain (%)
degree (°)
II (not micropeened)
III (one side micropeened)
IV (two sides micropeened)
μ_0H (T)

Fig. 10.

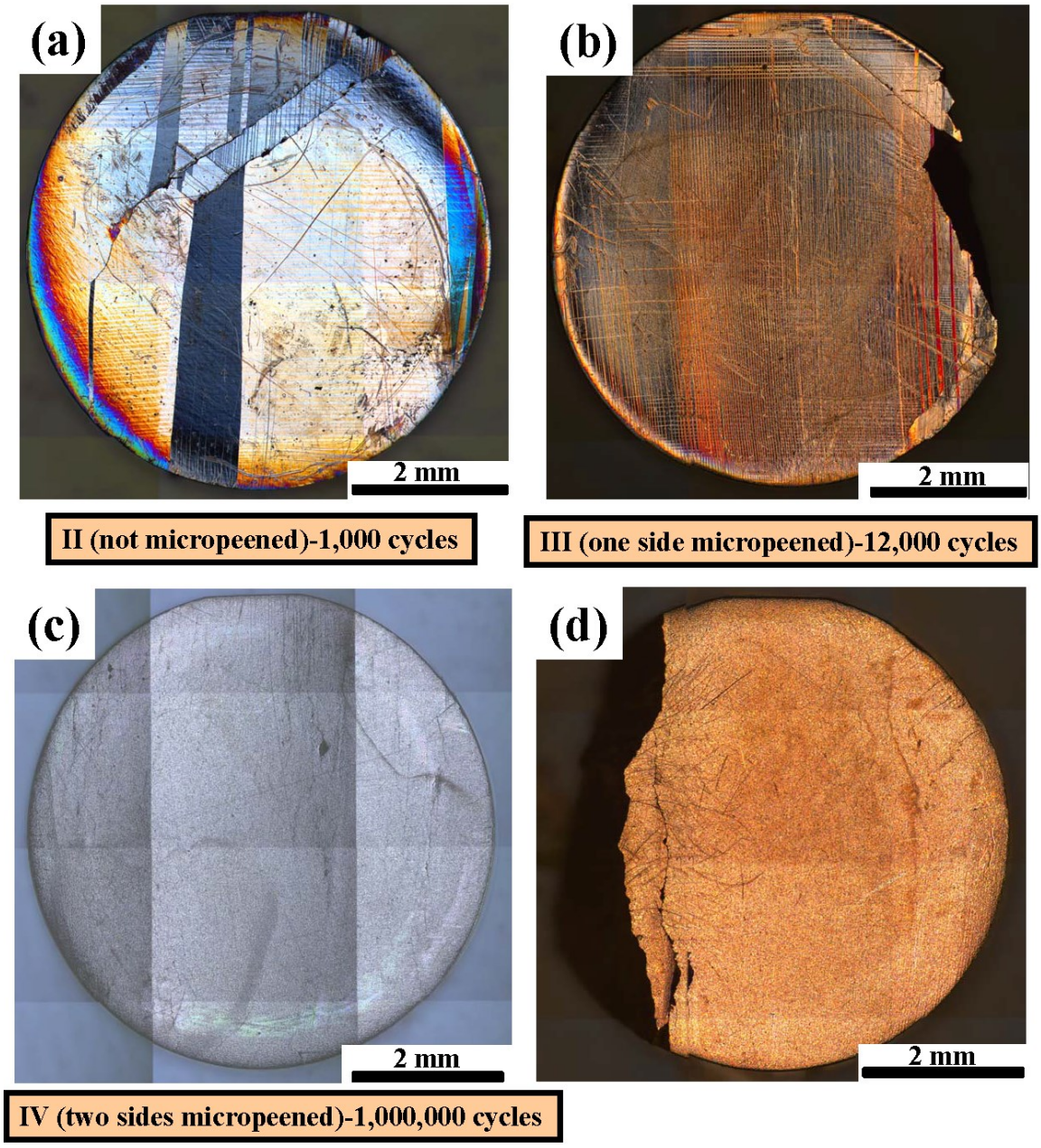
(a)
2 mm
II (not micropeened)-1,000 cycles
(b)
2 mm
III (one side micropeened)-12,000 cycles
(c)
2 mm
IV (two sides micropeened)-1,000,000 cycles
(d)
2 mm

Fig. 11.

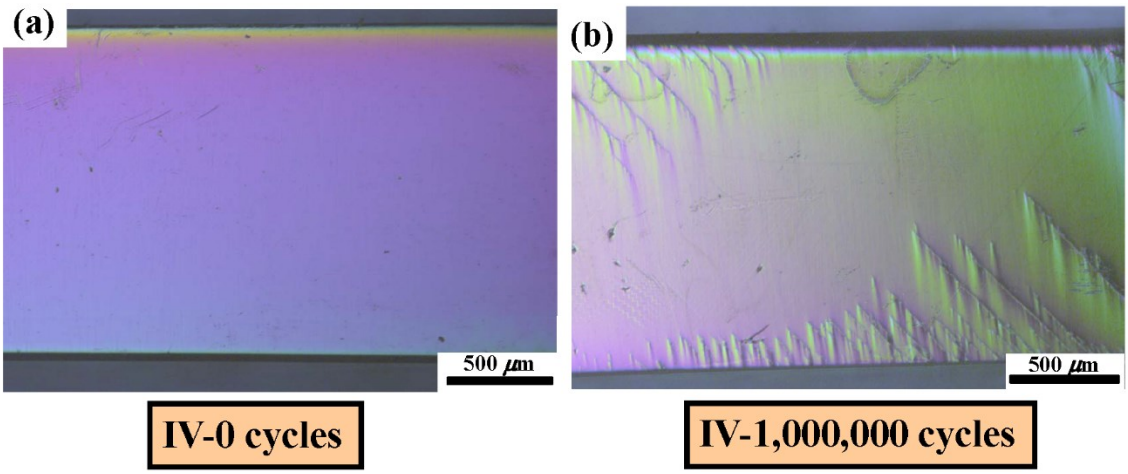

Fig. 12.

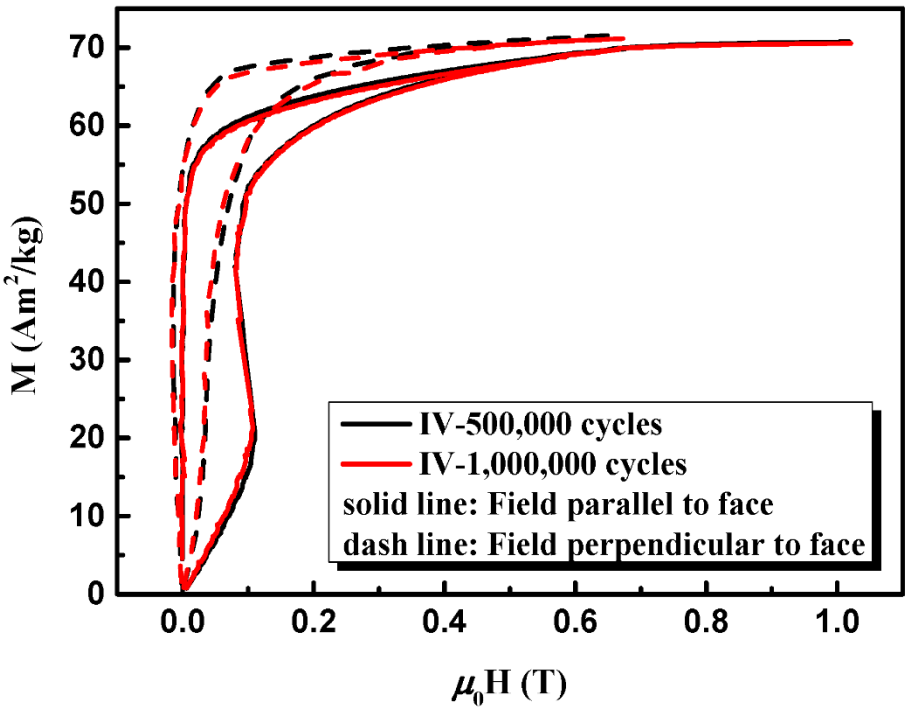
M (Am²/kg)
70
60
50
40
30
20
10
0
0.0
0.2
0.4
0.6
0.8
1.0
μ0H (T)
IV-500,000 cycles
IV-1,000,000 cycles
solid line: Field parallel to face
dash line: Field perpendicular to face

Fig. 13.

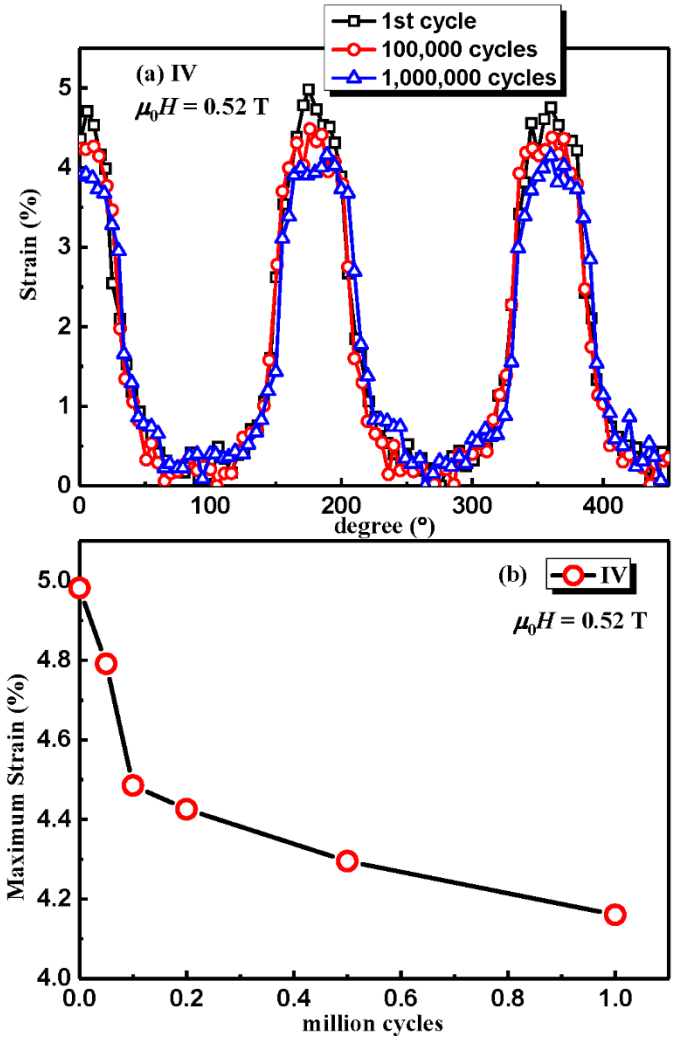
1st cycle
100,000 cycles
1,000,000 cycles
(a) IV
$\mu_0 H$ = 0.52 T
Strain (%)
degree (°)
(b) IV
$\mu_0 H$ = 0.52 T
Maximum Strain (%)
million cycles

Fig. 14.

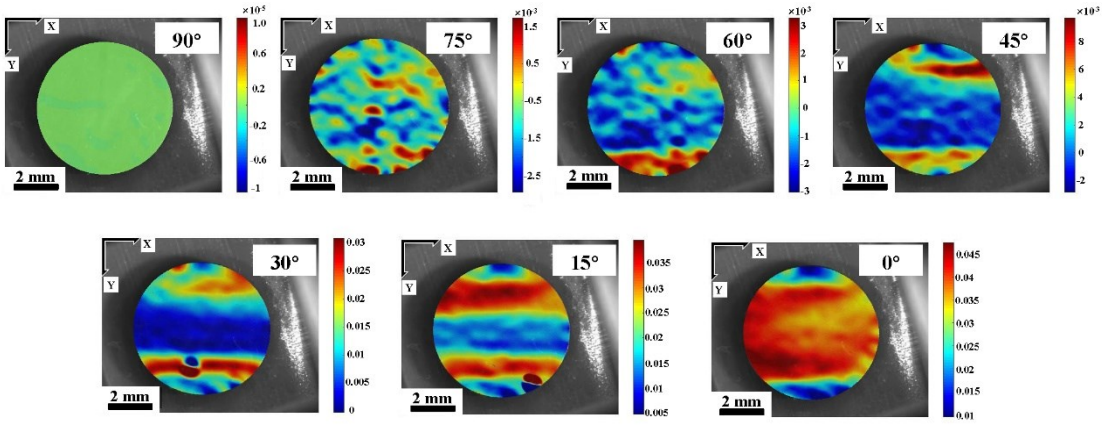

Fig. 15.

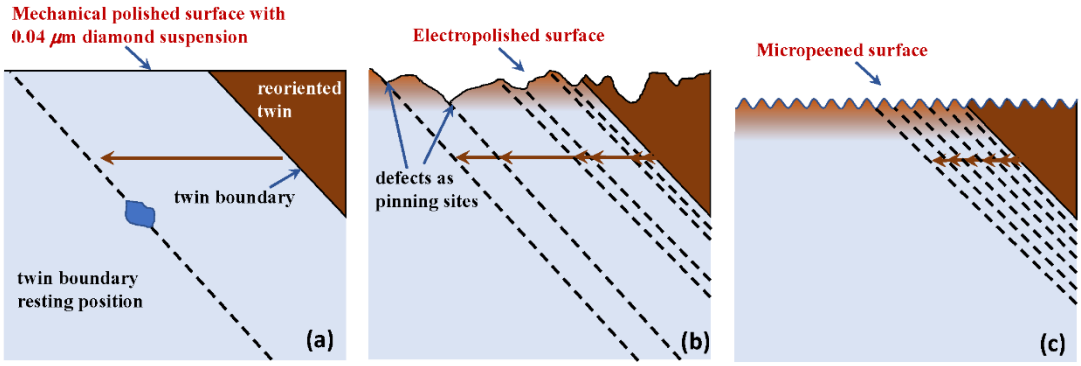
Mechanical polished surface with
0.04 μm diamond suspension
reoriented
twin
twin boundary
twin boundary
resting position
(a)
Electropolished surface
defects as
pinning sites
(b)
Micropeened surface
(c)

Fig. 16.